Research Article | Vol. 29, No. 18 / 30 Aug 2021 / Optics Express 29095

Optics EXPRESS

High precision integrated photonic thermometry enabled by a transfer printed diamond resonator on GaN waveguide chip

JACK A. SMITH,[1,2] PAUL HILL,[1,2] CHARALAMBOS KLITIS,[3] LUKAS WEITUSCHAT,[4] PABLO A. POSTIGO,[4] MARC SOREL,[3,5] MARTIN D. DAWSON,[1] AND MICHAEL J. STRAIN[1,*]

[1]*Institute of Photonics, Dept. of Physics, 99 George St., Technology and Innovation Centre, University of Strathclyde, Glasgow G1 1RD, UK*
[2]*Diamond Science and Technology, Centre for Doctoral Training, University of Warwick, Gibbet Hill Road, Coventry CV4 7AL, UK*
[3]*School of Engineering, University of Glasgow, Glasgow G12 8LT, UK*
[4]*Instituto de Micro y Nanotecnología, IMN-CNM, CSIC (CEI UAM+CSIC) Isaac Newton, 8, Tres Cantos, E-28760 Madrid, Spain*
[5]*Institute of Technologies for Communication, Information and Perception (TeCIP), Sant'Anna School of Advanced Studies, Via Moruzzi 1, 56127 Pisa, Italy*
[*]*michael.strain@strath.ac.uk*

Abstract: We demonstrate a dual-material integrated photonic thermometer, fabricated by high accuracy micro-transfer printing. A freestanding diamond micro-disk resonator is printed in close proximity to a gallium nitride on a sapphire racetrack resonator, and respective loaded Q factors of 9.1×10^4 and 2.9×10^4 are measured. We show that by using two independent wide-bandgap materials, tracking the thermally induced shifts in multiple resonances, and using optimized curve fitting tools the measurement error can be reduced to 9.2 mK. Finally, for the GaN, in a continuous acquisition measurement we record an improvement in minimum Allan variance, occurring at an averaging time four times greater than a comparative silicon device, indicating better performance over longer time scales.

1. Introduction

Photonic integrated circuits (PICs) are increasingly being implemented in a variety of sensing and metrology applications [1,2], with the often cited benefits being the reduction in size and cost because of the small form factor of photonic devices, as well as improvements in stability, robustness, and often sensitivity. Thermometry is an important application that could benefit from PIC implementation [3–6], owing to the importance of accurate temperature measurements across a number of fields, such as manufacturing [7], physiological monitoring [8,9], and environmental engineering controls [10,11]. Although inexpensive, electrical resistance based thermometers like the standard platinum resistance thermometer are sensitive to environmental conditions and require recalibration due to resistance drift over time [12]. There has been much work in developing photonic thermometers which are more robust to mechanical degradation and electromagnetic interference, with recent work utilizing silicon resonators (both microrings [3,5] and photonic crystal cavities [4]) which have high thermal sensitivities afforded by silicon's large thermo-optic coefficient. However, they are also more susceptible to long-term drift and absorption based self-heating [4], both due to two-photon absorption and surface state absorption [13], leading to inaccurate readings over longer time scales.

#433607 https://doi.org/10.1364/OE.433607
Journal © 2021 Received 8 Jun 2021; revised 11 Aug 2021; accepted 11 Aug 2021; published 25 Aug 2021
Corrected: 2 September 2021

Optics EXPRESS

These issues may be addressed through the use of alternative integrated material platforms; particularly those with wide-bandgaps [14]. Two such materials are gallium nitride (GaN) and diamond, whose respective band-gaps (3.4 eV and 5.4 eV) not only allow them to operate over large transparency windows, but also help alleviate the absorption based self-heating present in silicon devices. The thermal bistability present in some silicon devices [4,15] is also removed by designing devices to have larger mode volumes, and using materials with lower thermo-optic coefficients - such as GaN and diamond. Further, the use of resonators with high Q factors and well defined lineshapes [16] provides a more effective tool with which to probe the environment in the vicinity of the device.

Here we present a compact, dual material photonic device for optical thermometry, composed of the wide-bandgap materials diamond and GaN. By using two materials in a compact footprint, their independent thermo-optic coefficients will present different, but linearly correlated, wavelength shifts with temperature. Any environmental changes that lead to variations in either of the material's refractive indices will be highlighted by deviations from a linear correlation in their wavelength response. Furthermore, any drifts in device performance over time that result in changes to the thermo-optic coefficients will also be highlighted by changes to the linear correlation between the two materials. Our hybrid device consists of a transfer-printed diamond micro-disk resonator and a GaN on sapphire racetrack, in close proximity on chip. The resonators share a common bus channel, which is characterised from 1540 nm to 1600 nm, showing resonances with loaded Q factors of 2.9×10^4 and 9.1×10^4 for the GaN and diamond respectively. In a simultaneous thermal tuning approach, we are able to measure temperature shifts with an error of 9.2 mK, while also demonstrating temperature noise stabilities with reduced minimum Allan variances, occuring at an averaging time four times greater greater than a similar silicon racetrack resonator. The uncertainties of our measurement are reduced by tracking the shifts of multiple resonance peaks belonging to the two materials, where the position of each peak is in effect an independent measurement of the local temperature, sampled simultaneously by the two nearby resonators in one transmission sweep. Other methods to increase the number of peaks available for this form of multi-peak tracking include using devices with smaller free spectral ranges, or using cascaded resonators in a single material.

2. Device fabrication and characterization

The device comprises a GaN racetrack (coupling length 65 μm, bend radius 30 μm) and a diamond disk (radius 12.5 μm) sharing a common GaN waveguide bus. The device fabrication, outlined in Fig. 1, involves electron beam lithography in hydrogen silsequioxane (HSQ) negative resist, and inductively-coupled plasma (ICP) reactive-ion etching for both GaN and single crystal chemical vapour deposition diamond.

The GaN receiver chip consists of 650 nm of c-plane GaN grown on sapphire with a $\sim$ 350 nm aluminium nitride buffer layer, which is patterned with of an array of laterally coupled racetrack resonators of waveguide width 1 μm. After the HSQ mask is transferred to the GaN with an Ar/Cl_2 etch, residual resist is removed in a buffered oxide solution. Finally, the end portions of the chip are cleaved off to allow optical coupling to the waveguide facets with a lensed fiber.

Separately, single crystal CVD diamond is laser diced and polished from its as-grown dimensions to a 2 mm square, with an approximate thickness of 30 μm. Following previous work in our group on diamond lithography [17–19], the diamond is first cleaned in a piranha solution of three parts H_2SO_4 to one part H_2O_2, before being thinned to $\sim$1 μm in an Ar/Cl_2 etch, which also smooths the surface of the diamond to below 1 nm rms roughness. The diamond is then transferred with capillary-assisted bonding to a silicon chip readied with electron-beam alignment markers for the patterning step, again utilising HSQ resist. The etch chemistry used to transfer the pattern to the diamond is Ar/O_2, which unlike Ar/Cl_2 has a favorable selectivity

Optics EXPRESS

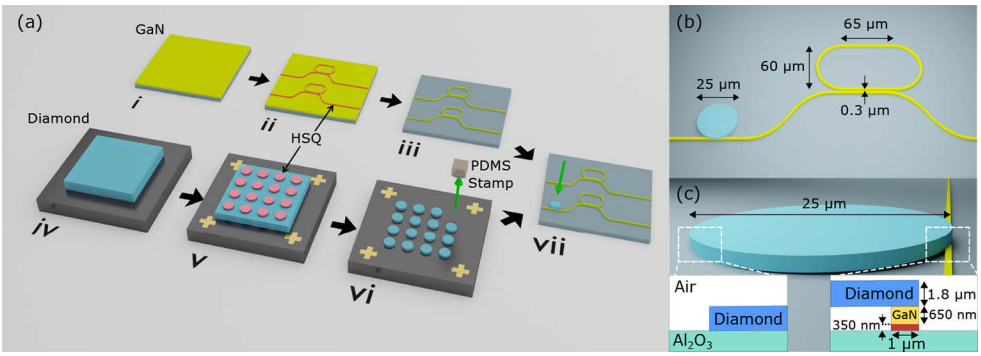

Fig. 1. (a) The parallel process flow: (i) The GaN wafer is (ii) patterned with HSQ e-beam resist and (iii) etched in an ICP-RIE using Ar/Cl_2 chemistry. (iv) The diamond is thinned to ~ 1μm - 2μm , also with an Ar/Cl_2 ICP etch before being (v) transferred to a silicon chip pre-patterned with e-beam alignment markers, whereupon HSQ is spun and patterned into disks. (vi) An Ar/O_2 ICP etch down to the silicon exposes the disks, before a disk of thickness 1.8 μm is (vii) transfer printed on to the GaN chip. (b) Device dimensions. (c) Cross-sectional dimensions, showing a total waveguide height of 1 μm consisting of 650 nm of GaN and 350 nm of AlN buffer layer.

between diamond and mask. The residual HSQ is removed with a CF_4/H_2 RIE etch, and the disk selected for printing has a thickness of 1.8 μm.

A NanoInk NLP2000 dip pen nanolithography tool, modified for micro-transfer printing, is used to assemble the final device (Fig. 2(b)). The tool consists of a stack of high precision motion control stages with an integrated optical microscope. The stage on which donor and receiver chips are mounted has five degrees of freedom - x, y, z, and two tilt axes [20]. An elastomeric polydimethylphenylsiloxane (PDMS) stamp (Fig. 2(a)), patterned with deformable pyramidal features [21,22], is mounted on the rigid connection between the microscope objective and the stage. During the printing process, the donor and receiver samples are brought into contact with the stamp through the relative motion of the substrate stage, which is fully controllable with the system software [23]. AFM line scans along the tops of disks of similar thickness printed in the same way show a linear height profile along the direction perpendicular to the waveguide, indicating the disk rests rigidly atop the guide, allowing vertical coupling to the disk's whispering gallery modes. Interference fringes visible in Fig. 2(c) indicates that a portion of the diamond is not in direct contact with the sapphire substrate.

Finally, the device is characterized with an end-fire fiber injection rig, shown in Fig. 3. An Agilent 8164B laser which is equipped with a single-mode fiber output passes light through a polarization isolator, before coupling to a polarization maintaining lensed fiber. By rotating this fiber we can excite either TE or TM modes in the waveguide. All results in this work correspond to TE mode injection. A microscope objective collects the light transmitted through the device and focuses it onto a photodetector and an imaging camera via a beam splitter. Transmission spectra are constructed by synchronously running a wavelength sweep on the laser, and taking a time trace of the voltage at the detector with an oscilloscope.

2.1. GaN racetrack transmission

An example GaN racetrack transmission spectrum is shown in Fig. 4(a). The resonator is single-mode, with a free spectral range (FSR) of ~3 nm, from which we calculated a group index, n_g, of 2.503, using:

$$n_g = \frac{\lambda^2}{FSR \times L}, \tag{1}$$

Optics EXPRESS

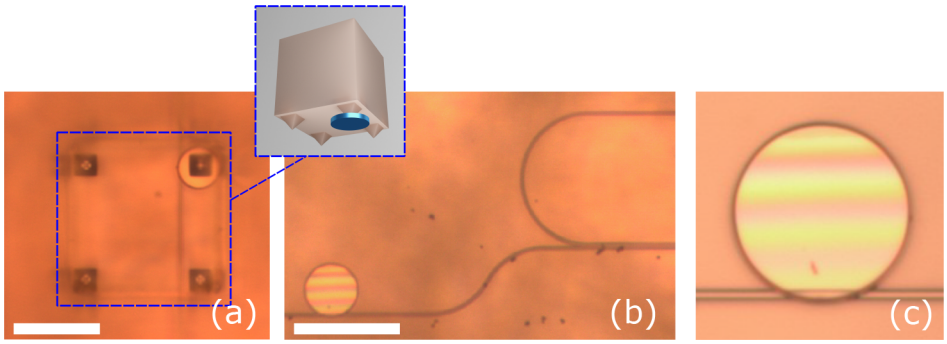

Fig. 2. Plan view optical micrographs of (a) PDMS stamp during the printing process, (b) the final device, and (c) detail of the printed diamond disk, with a diameter of 25 μm. All scale bars are 50 μm.

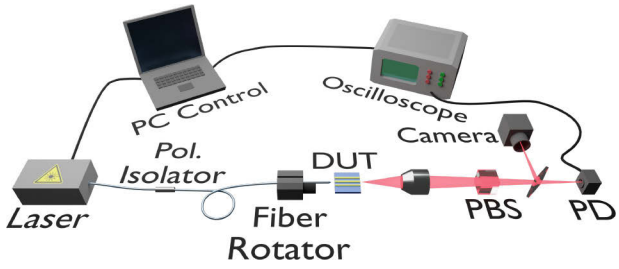

Fig. 3. Schematic of end-fire fiber injection rig used to optically characterize the devices. DUT: Device under test, PBS: Polarizing beamsplitter, PD: Photodiode.

where L is the cavity length. Resonance dips are fitted with a nonlinear least-squares method and the following all-pass transmission function [24]:

$$T_{pass} = \frac{a^2 + r^2 - 2racos(\phi)}{1 + (ra)^2 - 2racos(\phi)}, \tag{2}$$

where a is the single-pass field amplitude transmission, r is the self-coupling coefficient, and ϕ relates to the propagation constant β through $\phi = \beta L$. An example of such a fit is shown in Fig. 4(b), for a resonator of coupling length 30 μm, extracting a peak loaded Q factor of 2.9×10^4, and a mean loaded Q factor over 37 resonances and two nominally identical resonators of 2.6×10^4. From a, a minimum distributed loss of 3.13 dB/cm is calculated, which in addition to waveguide propagation loss, includes losses due to the coupling section. A peak intrinsic Q factor of 1.22×10^5 is found, calculated from the loaded Q and the normalised on-resonance transmission, T, and the following:

$$Q_{int} = \frac{2Q}{1 \pm T^{1/2}}, \tag{3}$$

where the summation (subtraction) is taken in the denominator in the case of under-coupling (over-coupling).

2.2. Diamond on GaN transmission

The channel on which the diamond disk is printed is characterized before and after the printing process (Fig. 5(a,b)). Because the GaN is single-mode its regularly spaced resonances can be easily distinguished from the additional diamond disk lines.

Optics EXPRESS

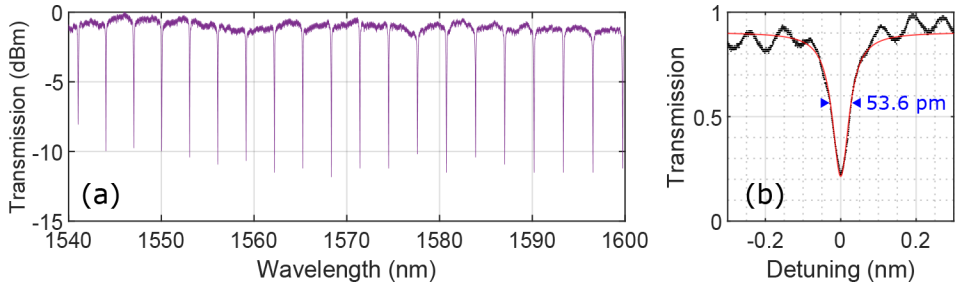

Fig. 4. (a) GaN racetrack transmission spectrum. (b) Example fit of a resonance at 1558.8437 nm.

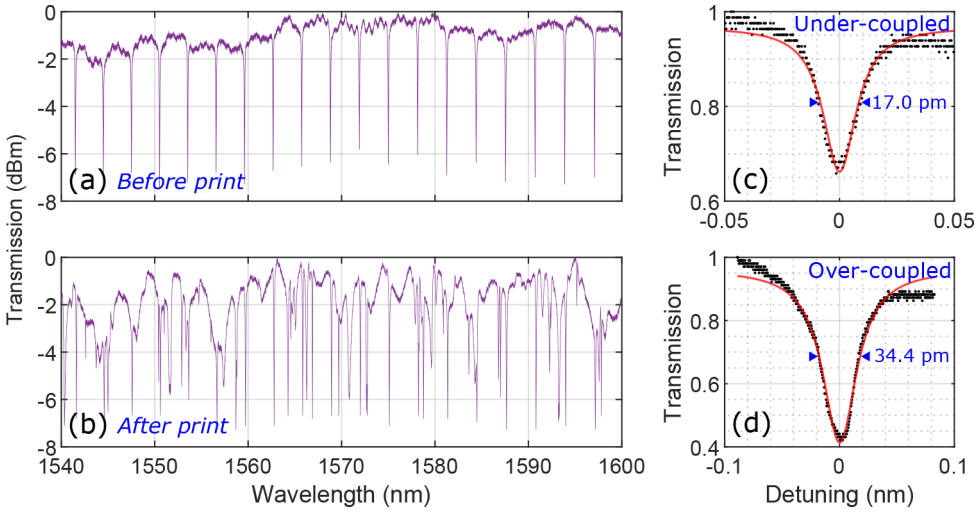

Fig. 5. (a) Receiver GaN spectrum before print. (b) The same spectrum after print, now featuring diamond resonances. (c) An under-coupled diamond resonance at 1542.6089 nm. (d) An over-coupled diamond resonance at 1550.4125 nm.

After printing, two diamond resonances, one under-coupled and one over-coupled, are shown in Fig. 5(c,d) respectively, with Q factors of 9.1×10^4 and 4.5×10^4. Finally, we extract distributed losses of 1.70 dB/cm and 4.39 dB/cm and intrinsic Q factors of 2.67×10^5 and 9.91×10^4 for the over-coupled and under-coupled fits respectively. Average loss and intrinsic Q values over 7 identifiable resonances are 3.51 dB/cm and 1.57×10^5. Related to the self-coupling coefficient, r, is the power cross-coupling coefficient, κ, given by $(1 - r^2)^{1/2}$. For the GaN peaks in Fig. 5(b) we calculate a mean power cross-coupling fraction of 4.6%. For the diamond, which features both under-coupled and over-coupled resonances, the power cross-coupling varies from 0.8% to 1.5%.

3. Hybrid device thermometry

In order to highlight the benefits of using a dual material, dual resonator device for tasks such as thermometry, we carry out both stability measurements in time and multi-peak tracking with temperature. The device is placed on on a Peltier heating module, bonded with thermal grease to aid heat transport. Once aligned to a waveguide facet as in Fig. 3, the fiber is fixed in place and a baffle enclosure is set up around the sample and fiber injection apparatus, thus minimising both airflow across the device and cantilever oscillations of the fiber tip affecting the optical transmission. Temperature is measured locally with a resistance thermometer. At

Optics EXPRESS

all points, the Peltier was in a positive bias condition, meaning it was at a higher temperature than the environment. When the Peltier was off, the ambient temperature measured was 293 K. Transmission spectra are taken for increasing Peltier voltages, where the time taken for one full spectra is 3 s, limited by the laser sweep speed of 20 nm/s.

The temperature-dependent resonance wavelength of a ring resonator thermometer is given by:

$$\lambda_m = \frac{n_{eff}(\lambda, T)L(T)}{m}, \tag{4}$$

where n_{eff} is the effective index of the circulating mode and m is the mode number. Formally, a shift in resonance wavelength for a temperature change ΔT is given by [3]:

$$\Delta\lambda_m = \left(\frac{\left(\frac{\partial n_{eff}}{\partial T}\right) + n_{eff}\left(\frac{\partial L}{\partial T}\right)\left(\frac{1}{L}\right)}{n_g} \right)(\Delta T \times \lambda_m) \tag{5}$$

The temperature dependence of the cavity length L is neglected as the thermal-expansion coefficient ($\partial L/\partial T$) is dominated by the thermo-optic coefficient ($\partial n_{eff}/\partial T$). Thus a temperature measurement amounts to the accurate determination of the resonant wavelength shift.

Figure 6(a) shows the red-shift of diamond and GaN peaks, with two nearby peaks highlighted in Fig. 6(b). The left peak is a diamond resonance, the right a GaN, and their relative shifts are plotted in Fig. 6(c) with a correlation coefficient approaching 1. Owing to diamond's smaller thermo-optic coefficient, its shift is approximately 0.23 times that of GaN. We can evaluate the thermo-optic coefficients directly by rearranging Eq. (5), and noting that the slope of a plot of $\Delta\lambda/\lambda$ against T will yield the thermo-optic coefficient scaled by the group index. GaN's group index has already been calculated to be 2.503, based on Eq. (1). For the multimode diamond, it is difficult to obtain a group index value from the FSR. Instead we can use the fit variables a and r, and the following [24]:

$$n_g = \frac{(1-ra)\lambda^2}{\pi L(ra)^{1/2}} FWHM^{-1}, \tag{6}$$

which yields a value of $n_g = 2.52$. With these, and plots of $\Delta\lambda/\lambda$ against T for each GaN and each diamond peak in the spectra (two of which are shown in Fig. 6(d,e)), we calculate mean thermo-optic coefficients of $\partial n/\partial T = 6.068 \times 10^{-5}\ K^{-1}$ and $\partial n/\partial T = 1.425 \times 10^{-5}\ K^{-1}$ for the GaN and diamond respectively, matching well literature values [25,26].

3.1. Resonance position determination

To best evaluate the resonant wavelength, we fit the lineshape with a simple Lorentzian in favor of Eq. (2). Doing so simplifies the extraction of the peak wavelength, as the Lorentzian is directly a function of centre wavelength. However, this value is also strongly influenced by the span of the fitting window and any asymmetry in the off-resonance background transmission levels. Therefore, in order to systematically and accurately extract the true resonant wavelength these factors need to be taken into account. Compare for example the improvements in the fit between Figs. 7(a) and (c), where the fit is weighted around the peak and the off-resonant background is fit with a third-order polynomial. The squared norm of the residuals around the peak centre are reduced by a factor of 11. For each peak in Fig. 6(b), the order of the polynomial background correction and span of the fitting window are parameterized in order to systematically extract each resonant wavelength.

In favor of Eq. (5), the following simpler analysis is used:

$$\lambda(T + \Delta T) = \lambda(T) + \frac{d\lambda}{dT}\Delta T, \tag{7}$$

which is valid over the temperature ranges measured here, where $d\lambda/dT$ can simply be considered the calibration of our measurement tool, including the dispersion present in the full analysis

Optics EXPRESS

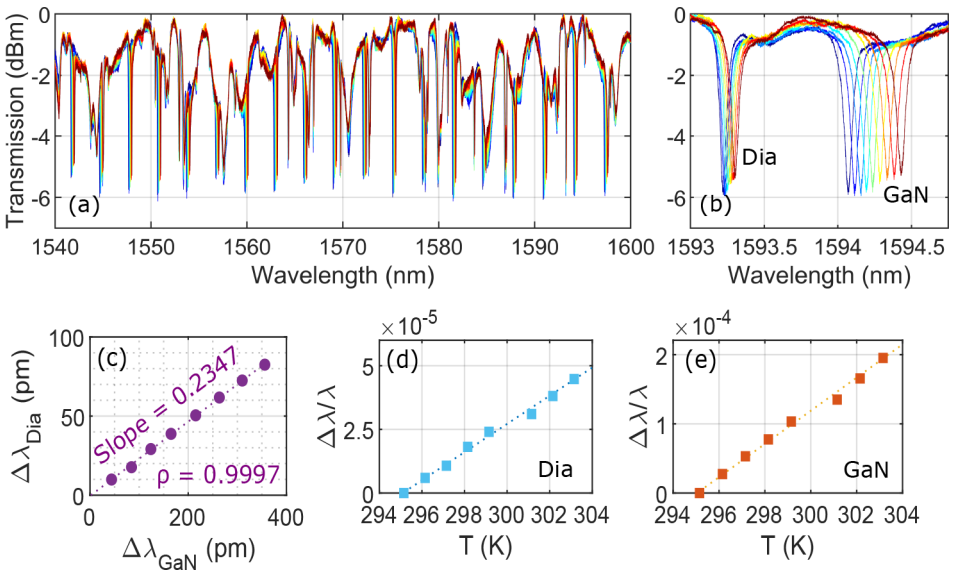

Fig. 6. (a) Thermally induced red-shifting of device transmission spectra. (b) Two nearby peaks, one diamond and one GaN. (c) Relative shifts of the mean values of the full sets of GaN and diamond peak positions. Peak shifts against temperature for the (d) diamond and (e) GaN.

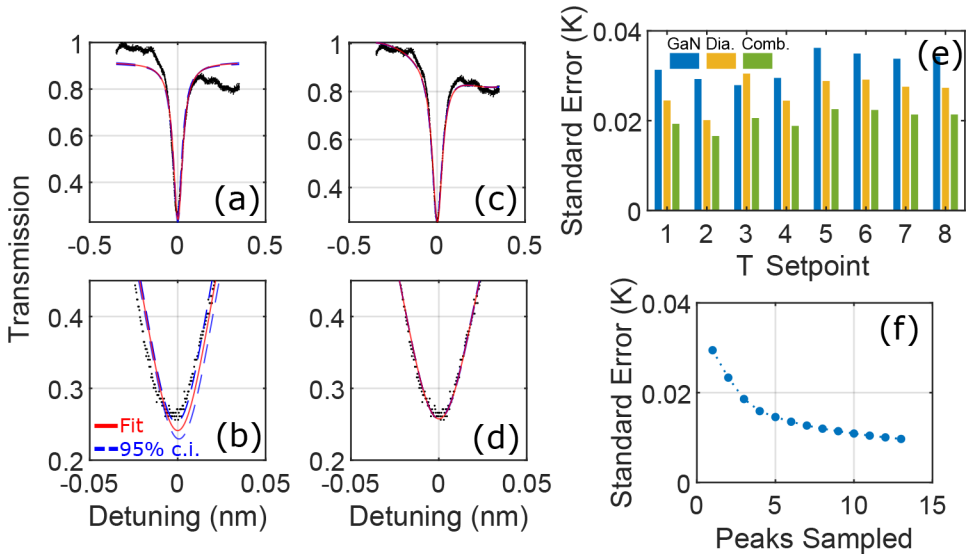

Fig. 7. (a) Lorentzian fit (red line) of the above diamond peak at 1593.22 nm with 95% confidence intervals (blue dashes). (b) Detail of the peak minimum. (c) The same Lorentzian fit, modified with fitting weights and a polynomial background correction. (d) Detail of the peak minimum, showing a much better fit. (e) Error in each temperature measurement using the GaN and diamond peaks shown in Fig. 6(a), with improved combined error. (f) Minimization of temperature errors by utilizing an increasing number of peaks from the spectra, taken for the second T setpoint in (e)).

Optics EXPRESS

of Eq. (5). Then, the magnitude of a temperature shift can be simply measured by accurate evaluations of resonance wavelength positions, and since we have multiple such independent measurements of the same temperature shift, the error is reduced. We have a wavelength shift given by:

$$\Delta\lambda = \lambda_2 - \lambda_1, \tag{8}$$

where $\lambda_2 = \lambda(T + \Delta T)$ and $\lambda_1 = \lambda(T)$. Their errors add in quadrature:

$$\sigma(\Delta\lambda) = [\sigma(\lambda_2)^2 + \sigma(\lambda_1)^2]^{1/2}, \tag{9}$$

where $\sigma(\lambda_{1,2})$ are the standard errors in the wavelength positions at T and $T + \Delta T$. These values are extracted from the Lorentzian fit variance-covariance matrix [27]. The temperature shift is calculated by rearranging Eq. (7) for ΔT:

$$\Delta T = \Delta\lambda \left(\frac{d\lambda}{dT}\right)^{-1}, \tag{10}$$

where $d\lambda/dT$ is the slope of that resonance's straight line fit calibration measurement (e.g. similar to those in Fig. 6(d,e)). Call that slope s. Following a simple propagation of errors, including the error in the straight line fits of the slope, s, the error in ΔT is found to be:

$$\sigma(\Delta T) = \Delta T \left[\left(\frac{\sigma(\Delta\lambda)}{\Delta\lambda}\right)^2 + \left(\frac{\sigma(s)}{s}\right)^2\right]^{1/2} \tag{11}$$

Finally, over all peaks, the combined weighted average is calculated with the following:

$$\Delta\overline{T} = \frac{\sum_{peaks} \Delta T/\sigma(\Delta T)^2}{\sum_{peaks} 1/\sigma(\Delta T)^2}, \tag{12}$$

with standard error given again by propagation of errors and found to be:

$$\sigma(\Delta\overline{T}) = \left[\frac{1}{\sum_{peaks} \sigma(\Delta T)^{-2}}\right]^{1/2}. \tag{13}$$

For the single pair of red-shifted GaN and diamond peaks shown in Fig. 6(a), the error in each temperature shift (peak position) is plotted in Fig. 7(e). The combined error in each shift takes the form of a weighted average of each material's individual measurement as in Eq. (13), and the improvement is evident in Fig. 7(e).

We see that the diamond in general performs better than the GaN in a single measurement due to its lower thermal-conductivity, and with a full characterization of each peak (for each material), the best accuracy in a 1 K temperature increase can be reduced to a value of 8.2 mK in Fig. 7(f), with an average over the 8 temperature set-points (c.f. Figure 6) of 8.7 mK. Finally, by noting that the correlation between the diamond and GaN peak shifts is near unity (Fig. 6(c)), it is possible to combine all wavelength shifts into a single set of values using the above slope of 0.2347 as a conversion factor. These combined values, and their associated temperatures are plotted in Fig. 8, which is well modelled by a second order polynomial function, whose mean fit residual (with standard error) is is 9.2 ± 1.8 mK - of the same order as the error estimate above. Thus by taking into account optimized fitting, the use of two independent wide-bandgap materials, and multiple peak averaging, there is a nearly fivefold improvement in accuracy compared to similar single peak silicon devices [4].

Optics EXPRESS

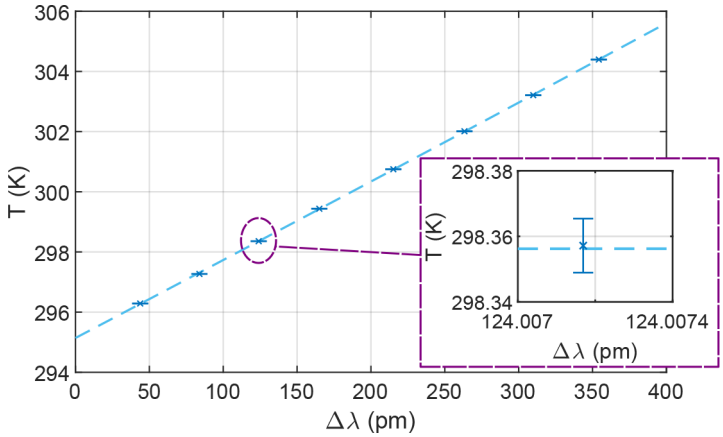

Fig. 8. Measured temperature against combined wavelength shift values, with error bars indicating the standard error in each temperature estimate.

3.2. *Stability measurement*

The frequency stabilities, which rely on the transient responses of each device, are now analyzed on an individual basis, and are not a combined steady-state measurement as above. To measure the long term stability of a resonant peak position a transmission spectrum is first taken to identify a suitable resonance. Then, following a similar method laid out in [3], the laser wavelength is parked on the side of the resonance, where the slope of the transmission function is greatest. Here, temperature fluctuations give the greatest fluctuations in the optical intensity transmitted through the chip. The laser is left running and a time trace of the light intensity transmitted through the chip is taken. A separate silicon chip featuring racetrack resonators of similar size and Q factor (coupling length 60 μm, bend radius 15 μm, waveguide width 500 nm) is used to compare and benchmark the diamond-on-GaN device. To account for the differences in on-chip optical power between the GaN and silicon (owing to a significant facet loss improvement of 16.11 dB for the silicon chip), the injected laser power is first attenuated before being launched

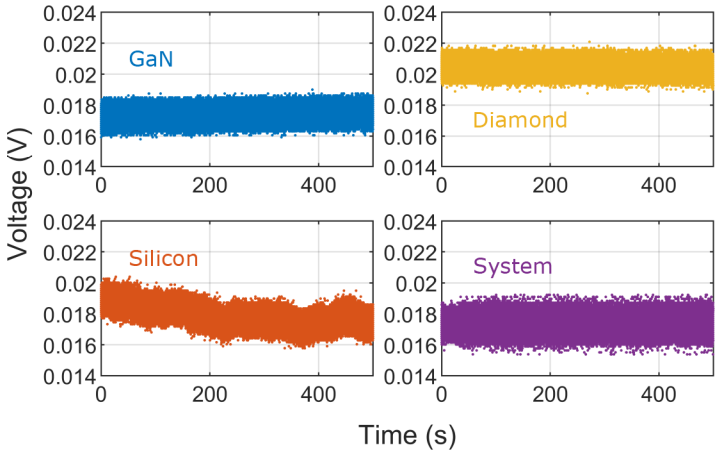

Fig. 9. Time traces of the intensity transmission with the laser parked on the side of a resonance for each material. Also included is the system noise trace.

Optics EXPRESS

into the silicon. This ensures an equal on-chip power for both chips, with a value of 4 μW. For these measurements, the Peltier was held at a constant 1 V (303 K).

Time traces, shown in Fig. 9, were taken for 500 s, with a sampling frequency of 4 kHz. The system noise trace was generated in the absence of a device chip in the optical path, with the injection fibre aligned directly to the collection optics (Fig. 3). The frequency analyses of these signals are shown in Fig. 10(a), which show the typical 1/f noise for low frequencies for each material. We note also improvements on these low frequency noise levels for the GaN and diamond over the silicon, with the diamond performing best. The noise floor is set by the total system noise (purple line, Fig. 10), which includes noise contributions from intensity fluctuations in the laser source. Allan variance plots (Fig. 10(b)) show a fourfold improvement in the minimum Allan variance averaging times of both diamond and GaN over the silicon, indicating improved sensor performance over longer time scales.

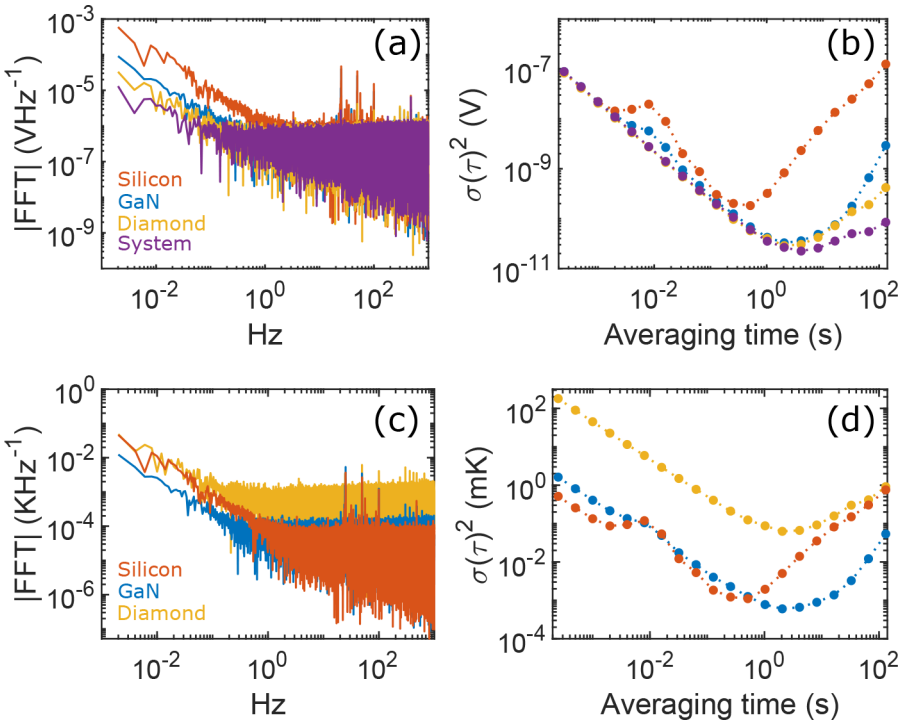

Fig. 10. (a) Fast Fourier transform amplitude spectra of the transmitted intensity time trace. (b) Allan variance plots for each resonator. (c) Equivalent FFT spectra in temperature units. (d) Allan variance plots of the temperature amplitude spectra.

While the diamond performs best in a like-for-like comparison of the through-chip intensity transmission, it is perhaps surprising that when the detector voltage traces are converted to an effective temperature trace the diamond performs poorly compared to the other materials. This conversion is done simply by taking the intensity trace as the codomain of a function (the side-of-fringe lineshape), whose domain is wavelength, or by Eq. (7), temperature. Since there is no such lineshape for the system trace, system noise cannot be included here. The diamond and GaN still share minimum Allan variance averaging times that are four times longer than the silicon, but now only the GaN features an improvement of the minimum Allan variance value itself. Previous work has shown that diamond disks printed onto SiO_2 are characterized by the strong confinement of heat to the diamond disk [19]. Other recent work has shown a significant barrier to thermal transport between Van der Waals bonded GaN on diamond [28].

Optics EXPRESS

These problems will be exacerbated by the presence of an air gap between the diamond and substrate as stated above, and the subsequent trapping of heat in the diamond is the likely source of the poorer diamond performance measured here.

4. Conclusion

We have demonstrated a dual material diamond-GaN photonic thermometry device. Our GaN photonic circuit features high Q factor resonators with low losses, and provides an excellent receiver platform for transfer-printed diamond components. For the GaN, in a continuous acquisition measurement we record an improvement in minimum Allan variance, occurring at an averaging time four times greater than a comparative silicon device, indicating better performance over longer time scales. In single-scan measurements, our dual-material dual-resonator approach decreases the measurement error to 9.2 mK by using simultaneous measurements of a temperature induced wavelength shift across the two materials, and multiple resonance peaks. This device was left air-clad, but future work could utilise a top cladding of SiO_2 or Al_2O_3 to encapsulate the sensing devices and protect them from longer term environmental changes that may also shift resonances. Furthermore, it should be possible to reduce errors further by utilising even higher Q factor devices, or more devices from other materials integrated in one sensor line.

Funding. Royal Academy of Engineering (Research Chairs and Senior Research Fellowships); Engineering and Physical Sciences Research Council (EP/L015315/1, EP/P013570/1, EP/P013597/1, EP/R03480X/1); PhotOQuant (EMPIR) (17FUN05).

Disclosures. The authors declare that there are no conflicts of interest related to this article.

Data Availability. All data underpinning this publication are openly available from the University of Strathclyde KnowledgeBase [29].

References

1. A. Hänsel and M. J. Heck, "Opportunities for photonic integrated circuits in optical gas sensors," JPhys Photonics **2**(1), 012002 (2020).
2. J. G. Wangüemert-Pérez, A. Hadij-ElHouati, A. Sánchez-Postigo, J. Leuermann, D.-X. Xu, P. Cheben, A. Ortega-Moñux, R. Halir, and Í. Molina-Fernández, "Subwavelength structures for silicon photonics biosensing," Opt. Laser Technol. **109**, 437–448 (2019).
3. H. Xu, M. Hafezi, J. Fan, J. M. Taylor, G. F. Strouse, and Z. Ahmed, "Ultra-sensitive chip-based photonic temperature sensor using ring resonator structures," Opt. Express **22**(3), 3098–3104 (2014).
4. N. Klimov, T. Purdy, and Z. Ahmed, "Towards replacing resistance thermometry with photonic thermometry," Sens. Actuators, A **269**, 308–312 (2018).
5. C. Zhang, G. Kang, Y. Xiong, T. Xu, L. Gu, X. Gan, Y. Pan, and J. Qu, "Photonic thermometer with a sub-millikelvin resolution and broad temperature range by waveguide-microring Fano resonance," Opt. Express **28**(9), 12599–12608 (2020).
6. S. J. Mihailov, "Fiber Bragg grating sensors for harsh environments," Sensors **12**(2), 1898–1918 (2012).
7. X. Y. Woo, Z. K. Nagy, R. B. Tan, and R. D. Braatz, "Adaptive concentration control of cooling and antisolvent crystallization with laser backscattering measurement," Cryst. Growth Des. **9**(1), 182–191 (2009).
8. M. R. Pinsky, L. Brochard, J. Mancebo, and G. Hedenstierna, *Applied physiology in intensive care medicine* (Springer, 2006).
9. C. A. Wunderlich, *On the temperature in diseases: a manual of medical thermometry*, vol. 49 (New Sydenham Society, 1871).
10. H. W. Stanford III, *HVAC water chillers and cooling towers: fundamentals, application, and operation* (CRC Press, 2011).
11. J. Turner, *Automotive sensors* (Momentum press, 2009).
12. G. F. Strouse, "Standard platinum resistance thermometer calibrations from the Ar TP to the Ag FP," NIST Special Publication **250**, 81 (2008).
13. F. Morichetti, S. Grillanda, M. Carminati, G. Ferrari, M. Sampietro, M. J. Strain, M. Sorel, and A. Melloni, "Non-invasive on-chip light observation by contactless waveguide conductivity monitoring," IEEE J. Sel. Top. Quantum Electron. **20**(4), 292–301 (2014).
14. L. M. Weituschat, W. Dickmann, J. Guimbao, D. Ramos, S. Kroker, and P. A. Postigo, "Photonic and thermal modelling of microrings in silicon, diamond and gan for temperature sensing," Nanomaterials **10**(5), 934 (2020).
15. Q. Xu and M. Lipson, "Carrier-induced optical bistability in silicon ring resonators," Opt. Lett. **31**(3), 341–343 (2006).

Optics EXPRESS

16. B. Hausmann, I. Bulu, V. Venkataraman, P. Deotare, and M. Lončar, "Diamond nonlinear photonics," Nat. Photonics **8**(5), 369–374 (2014).
17. C. Lee, E. Gu, M. Dawson, I. Friel, and G. Scarsbrook, "Etching and micro-optics fabrication in diamond using chlorine-based inductively-coupled plasma," Diamond Relat. Mater. **17**(7-10), 1292–1296 (2008).
18. P. Hill, E. Gu, M. D. Dawson, and M. J. Strain, "Thin film diamond membranes bonded on-demand with SOI ring resonators," Diamond Relat. Mater. **88**, 215–221 (2018).
19. P. Hill, C. Klitis, B. Guilhabert, M. Sorel, E. Gu, M. D. Dawson, and M. J. Strain, "All-optical tuning of a diamond micro-disk resonator on silicon," Photonics Res. **8**(3), 318–324 (2020).
20. B. Guilhabert, C. Klitis, J. McPhillimy, M. Sorel, M. Dawson, and M. Strain, "Nanoscale accurate heterogeneous integration of waveguide devices by transfer printing," in *2018 IEEE Photonics Conference (IPC)* (IEEE, 2018), pp. 1–2.
21. B. Guilhabert, A. Hurtado, D. Jevtics, Q. Gao, H. H. Tan, C. Jagadish, and M. D. Dawson, "Transfer printing of semiconductor nanowires with lasing emission for controllable nanophotonic device fabrication," ACS Nano **10**(4), 3951–3958 (2016).
22. A. Carlson, A. M. Bowen, Y. Huang, R. G. Nuzzo, and J. A. Rogers, "Transfer printing techniques for materials assembly and micro/nanodevice fabrication," Adv. Mater. **24**(39), 5284–5318 (2012).
23. J. McPhillimy, D. Jevtics, B. J. Guilhabert, C. Klitis, A. Hurtado, M. Sorel, M. D. Dawson, and M. J. Strain, "Automated nanoscale absolute accuracy alignment system for transfer printing," ACS Appl. Nano Mater. **3**(10), 10326–10332 (2020).
24. W. Bogaerts, P. De Heyn, T. Van Vaerenbergh, K. De Vos, S. Kumar Selvaraja, T. Claes, P. Dumon, P. Bienstman, D. Van Thourhout, and R. Baets, "Silicon microring resonators," Laser Photonics Rev. **6**(1), 47–73 (2012).
25. N. Watanabe, T. Kimoto, and J. Suda, "Thermo-optic coefficients of 4H-SiC, GaN, and AlN for ultraviolet to infrared regions up to 500° C," Jpn. J. Appl. Phys. **51**, 112101 (2012).
26. R. P. Mildren, "Intrinsic optical properties of diamond," *Optical Engineering of Diamond* (Wiley, 2013), pp. 1–34.
27. G. A. Seber and C. J. Wild, *Nonlinear Regression* (John Wiley & Sons, 2003), p. 63.
28. W. M. Waller, J. W. Pomeroy, D. Field, E. J. Smith, P. W. May, and M. Kuball, "Thermal boundary resistance of direct van der Waals bonded GaN-on-diamond," Semicond. Sci. Technol. **35**(9), 095021 (2020).
29. J. A. Smith, "Data for: High precision integrated photonic thermometry enabled by a transfer printed diamond resonator on a GaN waveguide chip," University of Strathclyde KnowledgeBase, 2021, https://doi.org/10.15129/f7404ca9-fd0e-4ef6-a8ad-8372f0ff52db.